

ARTICLE

DOI: 10.1038/s41467-017-02378-3

OPEN

Near-field spectroscopic investigation of dual-band heavy fermion metamaterials

Stephanie N. Gilbert Corder¹, Xinzhong Chen¹, Shaoqing Zhang², Fengrui Hu³, Jiawei Zhang¹, Yilong Luan³, Jack A. Logan¹, Thomas Ciavatti¹, Hans A. Bechtel⁴, Michael C. Martin⁴, Meigan Aronson⁵, Hiroyuki S. Suzuki^{6,10}, Shin-ichi Kimura^{7,11}, Takuya Iizuka^{7,12}, Zhe Fei³, Keiichiro Imura^{7,8}, Noriaki K. Sato⁸, Tiger H. Tao^{2,9} & Mengkun Liu¹

Broadband tunability is a central theme in contemporary nanophotonics and metamaterials research. Combining metamaterials with phase change media offers a promising approach to achieve such tunability, which requires a comprehensive investigation of the electromagnetic responses of novel materials at subwavelength scales. In this work, we demonstrate an innovative way to tailor band-selective electromagnetic responses at the surface of a heavy fermion compound, samarium sulfide (SmS). By utilizing the intrinsic, pressure sensitive, and multi-band electron responses of SmS, we create a proof-of-principle heavy fermion metamaterial, which is fabricated and characterized using scanning near-field microscopes with <50 nm spatial resolution. The optical responses at the infrared and visible frequency ranges can be selectively and separately tuned via modifying the occupation of the 4f and 5d band electrons. The unique pressure, doping, and temperature tunability demonstrated represents a paradigm shift for nanoscale metamaterial and metasurface design.

¹ Department of Physics and Astronomy, Stony Brook University, Stony Brook, NY 11794, USA. ² Department of Mechanical Engineering, University of Texas-Austin, Austin, TX 78712, USA. ³ Department of Physics and Astronomy, Iowa State University, Ames, IA 50011, USA. ⁴ Advanced Light Source Division, Lawrence Berkeley National Laboratory, Berkeley, CA 94720, USA. ⁵ Department of Physics and Astronomy, Texas A&M University, College Station, TX 77843, USA. ⁶ National Institute for Materials Science, Tsukuba 305-0047, Japan. ⁷ UVSOR Facility, Institute for Molecular Science, Okazaki 444-8585, Japan. ⁸ Department of Physics, Nagoya University, Nagoya, Japan. ⁹ State Key Laboratory of Transducer Technology, Shanghai Institute of Microsystem and Information Technology, Chinese Academy of Sciences, Shanghai 200050, China. ¹⁰ Present address: Institute for Solid State Physics, University of Tokyo, Kashiwa 277-8581, Japan. ¹¹ Present address: Graduate School of Frontier Biosciences and Department of Physics, Osaka University, Suita, Osaka 565-0871, Japan. ¹² Present address: Toyota Technological Institute, Nagoya 468-8511, Japan. Correspondence and requests for materials should be addressed to S.N.G.C. (email: stephanie.gilbertcorder@stonybrook.edu) or to M.L. (email: mengkun.liu@stonybrook.edu)

Typically composed of composite systems with artificial subwavelength structures or inclusions, metamaterials (MM) were first introduced to supplement or replace naturally occurring solids where the electromagnetic response is limited by the inherent properties resulting from the electronic band structure^{1–3}. Recent developments, however, have embraced a reverse trend in which the intrinsic optical properties of natural materials are employed to aid in the design of new generations of MM devices⁴. This is especially relevant in the construction of switchable or tunable MM with dynamic control. For example, MM hybridized with phase-change materials such as transition metal oxides (vanadium oxides)^{5,6}, tunable 2D materials (graphene)⁷, and chalcogenide glasses ($\text{Ge}_2\text{Sb}_2\text{Te}_3$)⁸ have been explored extensively for this cause.

One major subset of phase-change materials is the strongly correlated electron systems (SCES), in which the competing electron–electron and electron–lattice interactions result in a high susceptibility to small external stimuli. A massive redistribution of the spectral weight over a broad frequency range can occur in SCES under strain, doping, or thermal excitation. So far, tunable MM design has mainly focused on altering/tuning the response of noble-metal resonators in composite devices by relying heavily on the single band electron properties of the SCES as functional substrates^{5,6,8–10}.

In this work, we demonstrate a unique route to creating dual-band plasmonic MM comprising a single strongly correlated heavy fermion system. We control and monitor the plasmonic response of not only d-band electrons, as in noble metals or transition metal oxides, but also of f-band electrons. This is achieved by utilizing the local phase transition in samarium sulfide (SmS), a canonical correlated heavy fermion system with 5d and 4f electrons. The application of modest pressure (6.5 kbar^{11,12}) turns the optically black semiconductor into a golden semi-metal and is accompanied by a broad spectral weight redistribution^{13,14}. By taking advantage of this pressure-dependent insulator to metal phase transition (IMT), we are able to write a conducting pattern on the material surface using an atomic force microscope (AFM) in ambient conditions without the need of a lithographic mask, metal deposition, extended sample preparation, or high vacuum requirements. Through controlled local distribution of pressure at the nanoscale and MM design, we are able to alter carrier occupations of the two energy bands and engineer the effective carrier density at the sample surface, giving rise to plasmonic resonances in the IR and visible regions. A combination of near-field and far-field optical techniques enables us to characterize the nanoscale phase separation and probe the electromagnetic response of the resulting devices from submicroscopic to macroscopic scales.

Results

Origin and spatial engineering of the dual-band resonances.

The phase diagram of SmS as a function of pressure and temperature is shown schematically in Fig. 1a (after^{14,15}). At ambient pressure, the semiconducting black phase of SmS has a direct band gap of ~ 0.4 eV and an indirect gap of ~ 0.09 eV^{13,15}. The Sm 4f⁶ states are highly localized such that the overlap between these electron wavefunctions vanishes and no plasma resonance exists in spite of the high 4f electron concentration¹⁶. With increasing pressure (crystal field splitting), SmS undergoes an isostructural phase transition to a golden intermediate valence (IV) state: from Sm^{2+} to a fractional valence of $\text{Sm}^{2.6-2.8+}$. This intermediate valence is a result of the 5d t_{2g} conduction band shifting lower in energy and hybridizing with the 4f⁶ band on the neighboring atomic site. As the valence changes, carriers move from the highly localized 4f⁶ state into the 5d t_{2g} conduction band¹⁷. These

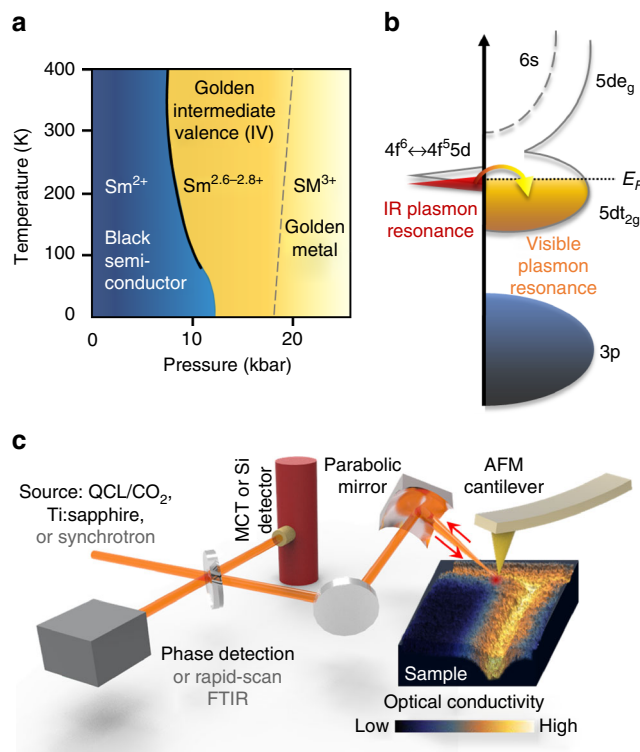


Fig. 1 Material properties of SmS and a schematic of the nano-spectroscopy and nano-imaging setup. **a** Phase diagram of samarium sulfide (SmS) as a function of pressure and temperature. The material undergoes a black to golden optical phase transition as the occupation of the valence states of the material change with applied pressure. **b** Diagram of golden IV phase of SmS after Batlogg et al.¹¹. The IR plasmon resonance is attributed to carriers in the 4f states, while the visible resonance is due to 5d carriers¹⁶. As pressure increases, the 4f electrons move into the 5d t_{2g} state as indicated by the arrow¹⁷. **c** AFM nano-lithography is performed on the SmS sample surface, producing a region of controlled strain defined by the AFM tip radius. The resulting pattern (shown in false color) is subsequently probed with scattering-scanning near-field optical microscopy (s-SNOM) to measure the optical changes. A laser-based or synchrotron light source is used to probe the near-field optical response at visible or IR frequencies

former f electrons (now in the d band) have residual interactions with the holes left behind, producing excitonic correlations¹⁸. In the golden IV phase, two distinct plasmon resonances exist, corresponding to light d (visible plasmon mode) electrons and heavy f (IR plasmon mode) electrons, shown schematically in Fig. 1b¹⁶. Above 20 kbar, the system becomes fully metallic (Sm^{3+}), the 4f resonance disappears as the gap collapses, and the 5d t_{2g} band is filled with 4f electrons¹⁷. For more details on the material properties, please see Supplementary Note 1.

In order to transform a bulk SmS single crystal into a reflective MM, we use contact mode AFM lithography to fabricate a series of surface structures. A conventional AFM tip writes a pre-defined pattern with controllable local pressure of ~ 5 – 15 kbar (calculated from force–distance curves) with 20 nm precision and 50 nm linewidth, as schematically illustrated in Fig. 1c and discussed in Supplementary Notes 2 and 3. This induces a local IMT in SmS, resulting in a color change from black to golden together with a large spectral weight shift in the visible and IR^{13,14}. The metallic volume fraction on the material surface can thus be selectively modified from 0 to 100%, facilitating nanoscale pattern formation. In contrast to previous demonstrations of “sketching” oxide heterostructures with voltage pulses¹⁹, the

method discussed here does not require the fabrication of electrodes or the application of an electrical voltage. Scattering-type scanning near-field optical microscopy (s-SNOM) techniques are sequentially employed to investigate the strain-induced IMT at the nanoscale. The s-SNOM method enables nano-imaging²⁰ and nano-spectroscopy^{21,22} which can locally probe (with resolution on the order of the AFM tip diameter) the resultant optical response of the tip-patterned region, thus verifying the presence of the metallic volume fraction at the sample surface after tip lithography (Fig. 1c). See Supplementary Note 4 for further details on the s-SNOM technique.

Near-field characterization of the dual-band resonances. Using AFM lithography, we pattern a gradient MM with decreasing line spacing from 412 to 163 nm as seen in the topography image of Fig. 2a. A visible red-golden color gradient can be immediately observed following the lithography process under a far-field white light camera (Fig. 2b). To understand the origin of this macroscopic color change, subsequent near-field imaging at 1.7 eV is performed to probe the contribution of the 5d t_{2g} band electrons. As shown in Fig. 2c, the blue and golden colors indicate semiconducting and conductive responses, respectively. The unpatterned regions above and below the MM show little signal (and indeed between the lithographic lines as well), confirming the lack of free carriers in the 5d conduction band prior to patterning.

With the exception of the largest spacing (442 nm), the near-field signal is consistent for all spacings at 1.7 eV, indicating the change in the visible color in the far-field image (therefore areal averaged free carrier density) is solely determined by the line spacing rather than an actual gradient in the occupation of the d-electron band. In contrast, IR near-field imaging reveals a local electronic response different from that at 1.7 eV: at 112 meV, for example, the highest near-field signal is not at the lower end of the grating MM but one color step above, as shown in Fig. 2d. At 112 meV, we are monitoring the delocalization of the 4f electrons while in the visible range only the 5d electrons are probed. In order to better understand the IR near-field response, we also perform IR broadband nano-spectroscopy as detailed below.

Figure 2e shows the near-field amplitude (S_3) image of a $1 \mu\text{m}^2$ region of a grating MM at 188 meV (1515 cm^{-1}). The surface nano-structure is probed with ultra-broadband nano-spectroscopy in three 20 nm locations designated in Fig. 2e: the region of maximum local strain (1), a transition region adjacent to the maximum strain (2), and an unstrained region (3). The results are shown in Fig. 2f, g, where the broadband near-field amplitude is normalized to a thin film gold reference^{22,23}. The lithographically strained regions (1) and (2) show an increase in far infrared reflectivity, indicating the patterned areas have a stronger broadband metallic response when compared to the semiconducting unstrained region (3). The peak in Fig. 2f around 58 meV (468 cm^{-1}) is attributed to an exciton near the indirect bandgap

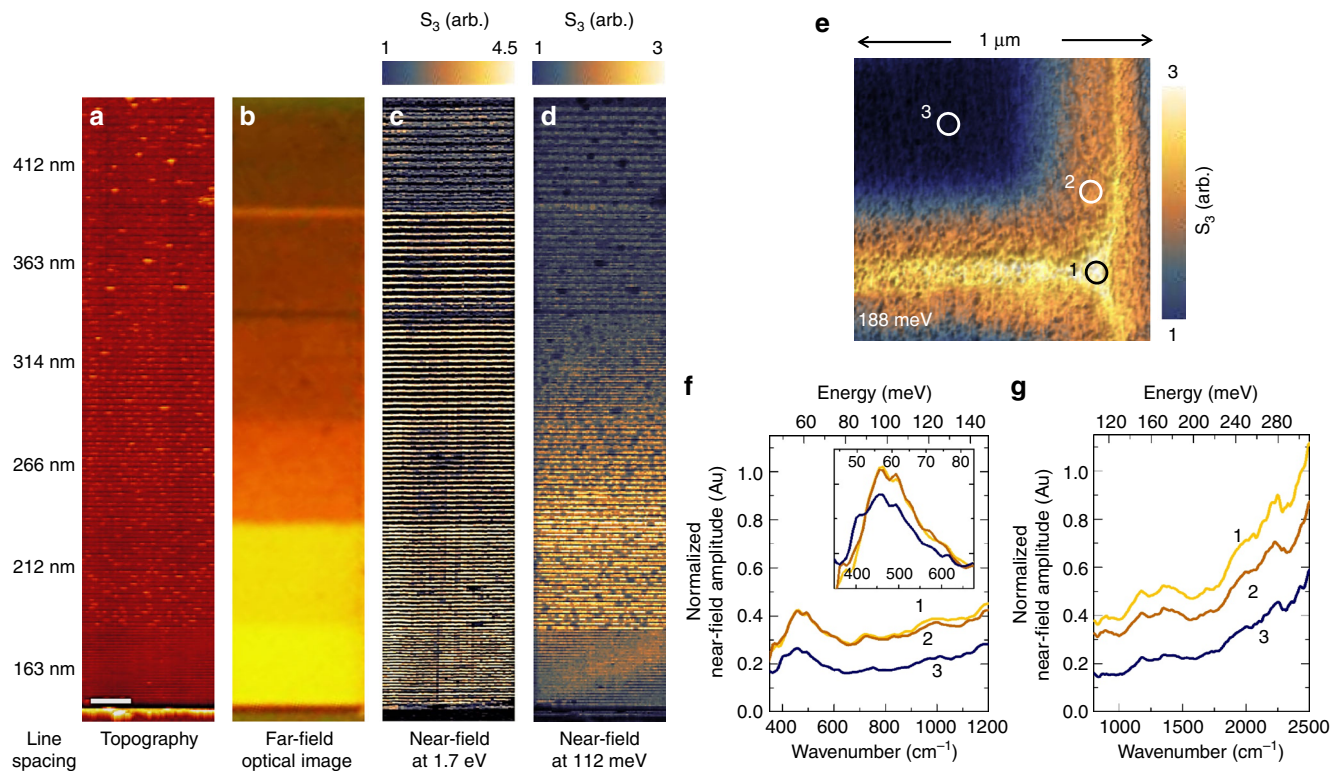


Fig. 2 IR and visible near-field characterization of SmS metamaterials created via AFM lithography. **a** The topography of a color gradient MM with decreasing spacing between the patterned lines (listed on the left) is shown for a depth of ~ 12 nm. The scale bar is 500 nm. A far-field optical image of the same gradient MM is shown in **b**; the color change from red to golden is achieved by altering the lithographic line spacing. Room-temperature near-field images are collected at 1.7 eV (**c**), and 112 meV (**d**). The near-field 3rd harmonic amplitude is shown in false-color, where blue indicates regions of semiconducting conductivity and gold indicates regions of metallic conductivity. **e** The near-field amplitude at 188 meV (1515 cm^{-1}) and 295 K is shown in false color for a $1 \mu\text{m}^2$ region of a grating pattern. The near-field amplitude change of the patterned area (in gold) is normalized to the semiconducting response (in blue). Three locations are marked in the image, indicating golden IV (1), transition (2), and semiconducting (3) regions of the MM. Broadband near-field spectroscopy (normalized to a gold thin film) at 295 K is shown in **f, g**, for the locations specified in the $1 \mu\text{m}^2$ image, indicating the presence of the localized golden IV phase on the surface of the SmS. The exciton peak at 58 meV (468 cm^{-1}) is observable in all three regions. The inset in **f**, shows the exciton peaks with the background removed to highlight the slight frequency shift with applied pressure

of SmS (around 87 meV or 700 cm^{-1})¹³ and the gentle slope at higher frequencies indicates the onset of the $4f^6-5d\ t_{2g}$ absorption edge¹¹. The inset in Fig. 2f illustrates the shift of the exciton peak to slightly higher frequencies¹³ and the baseline reflectivity increases significantly with the lithographic strain: the application of pressure causes the $5d\ t_{2g}$ band to shift lower in energy relative to the $4f$ band, and f electrons are transferred into the hybridized state, increasing the baseline reflectivity without changing the spectral features^{13,17,24}. The small peaks present between 700 and 2500 cm^{-1} are likely intra- $4f^5$ transitions, which become increasingly infrared active with applied pressure¹⁶. The presence of the exciton peak and indirect band gap between the $4f^6$ and $5d\ t_{2g}$ bands indicates that the golden phase produced by the patterning is still in the IV regime, and therefore we have access to plasmon resonances in both the $4f$ and $5d$ energy bands. This is not immediately clear from the fabrication process as the fully metallic and IV states are identical at visible frequencies—the plasmon resonance of the $5d$ conduction band gives rise to the golden color and is present in both IV and fully metallic SmS.

In Fig. 2e–g, the existence of a transition region demonstrates that the effects of the strain on the lattice extend beyond the lithography. Therefore, we attribute the increase in signal strength as line spacing decreases from 412 – 212 nm in Fig. 2d to an accumulation of local strain, which produces increasing overlap of the $4f$ electronic states and results in a stronger plasmonic resonance up to a threshold. As the population of carriers in the $4f$ band is reduced with increasing pressure, the strength of the $4f$ resonance ultimately decreases as can be seen in Fig. 2d for the 163 nm spacing. Since the depopulation of the $4f$ band occurs as a function of local strain and not necessarily at the same location as the smallest line spacing, the optical responses in the visible and IR range can be modulated independently—this will be further explored with a doped SmS MM. Therefore, we conclude that the far-field color gradient primarily arises from the differences in line spacing, resulting in the observed golden, orange, and red

optical colors. The $4f$ electron plasmonic resonance does not play a role in determining the apparent color, but displays a strong dependence on the local strain.

Far-field characterization of the dual-band resonances. Broadband control of the visible plasmon resonance is demonstrated through effective carrier density-tuning of the far-field MM response in Fig. 3a. By adjusting the periodicity of the lithographic lines, we tune the visible reflectivity of the MM from gray (unpatterned semiconducting) to red or golden. The reflectivity of golden MM grating has a strong response in the yellow and orange portions of the spectrum (~ 1.98 – 2.2 eV), but drops quickly in the red region ($\sim 1.6\text{ eV}$), giving rise to the golden color. The red MM grating is highly reflective below 1.8 eV . The reflectivity minima observed in all three spectra are due to the phonon-coupled plasmon edge, which also produces the steep reflectivity change in the visible^{11,14,16}. Details of the far-field measurements are discussed in Supplementary Notes 5 and 6. The spectra are fit with the Drude model of the dielectric function (dashed curves in Fig. 3; the model parameters can be found in Supplementary Note 7) to illustrate the plasma frequency shift to higher frequencies with increased lithographic line periodicity; indicating the effective free carrier population, N , is increasing. The effective plasma frequency values ω_p obtained from the Drude fits are 1.81 eV ($14,600\text{ cm}^{-1}$), 1.93 eV ($15,550\text{ cm}^{-1}$), and 2.16 eV ($17,450\text{ cm}^{-1}$) for the unpatterned semiconductor, red MM, and golden MM spectra, respectively. The fully metallic golden ω_p value is reported to be 2.45 eV ¹¹.

In addition to pressure tuning, the broadband IR reflectivity can be altered by changing the metallic fraction within the MM as well. To demonstrate, four distinct $20 \times 20\ \mu\text{m}$ regions are investigated in Fig. 3b (solid lines): an unpatterned semiconducting region, a polished metallic region, and two lithographically patterned structures—fishnet and grating MM. The fishnet MM consists of

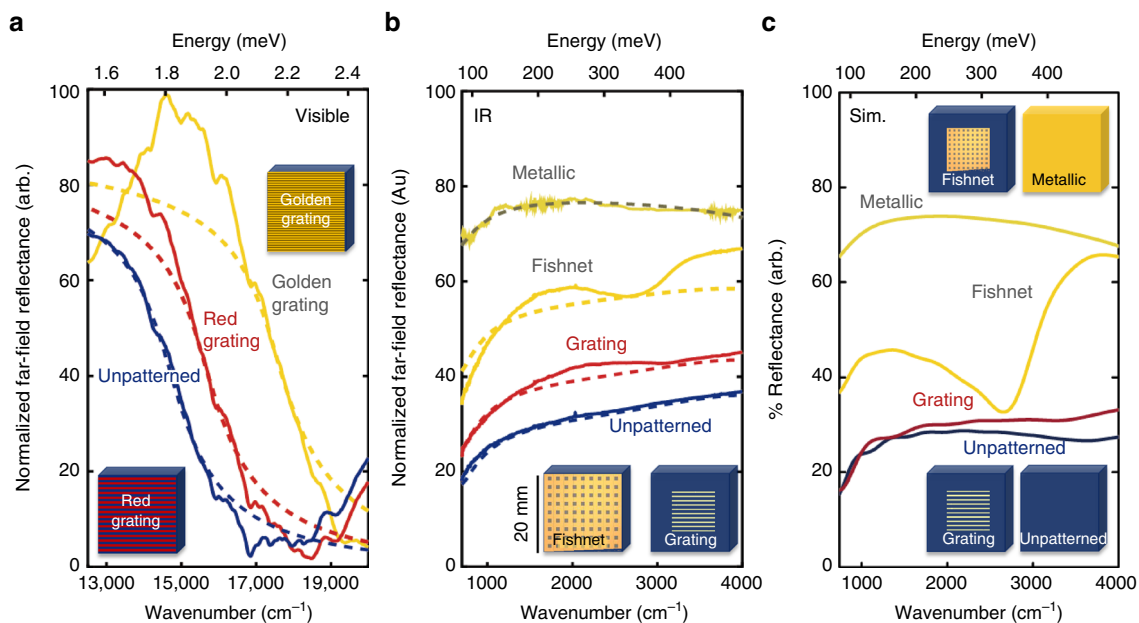


Fig. 3 Tuning the far-field response of SmS metamaterials in the visible and IR range. **a** Reflectance spectra (solid lines) of golden visible MM grating and red visible MM grating, compared to an unpatterned semiconducting reference at 295 K. The data are fit (dashed lines) using the Drude dielectric model, which shows the shift of the plasma edge. **b** IR spectra (solid lines) of a fishnet and grating MM as well as reference unpatterned semiconducting and metallic (golden) surfaces at 295 K. The data are fit using effective medium theory (dashed lines), indicating the overall reflectance change is a function of metallic fill fraction. Schematics of the $20 \times 20\ \mu\text{m}$ regions of the fishnet (lower left) and grating (lower right) are shown in the inset. **c** CST simulations of the experimental data in **b**, reproducing the peaks observed in the MM structures. Schematics of the four simulated regions are shown as insets

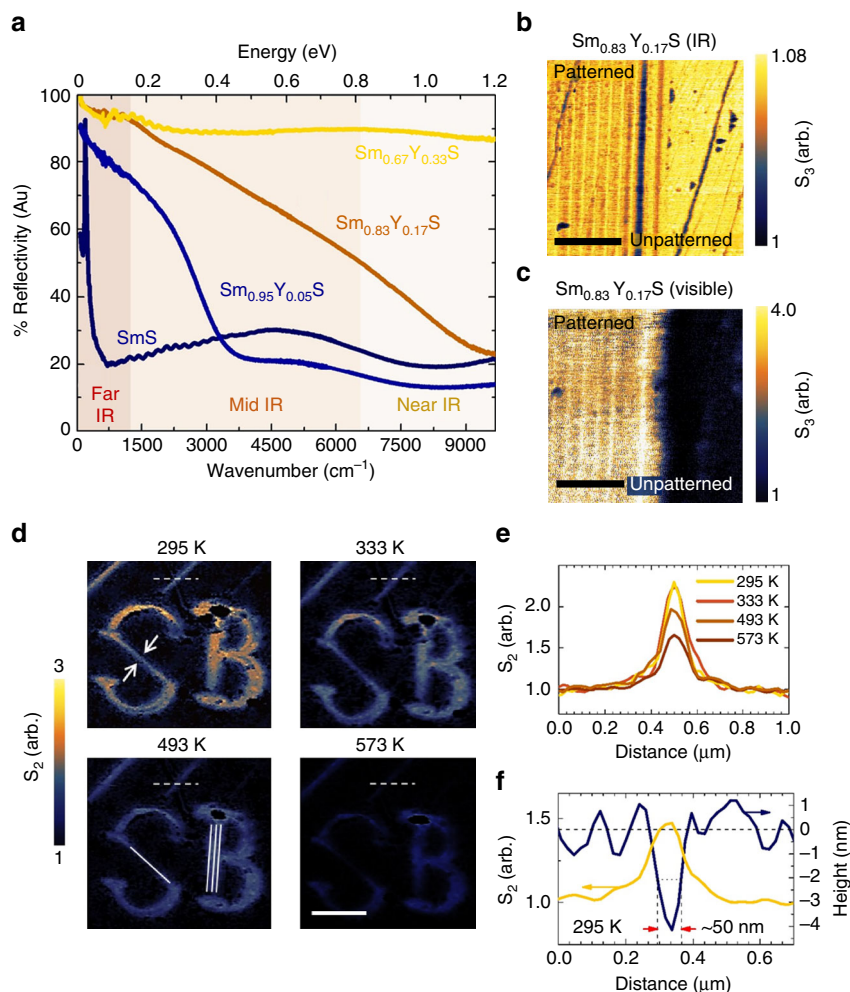


Fig. 4 Dopant and temperature tuning of the near-field reflectivity. **a** Far-field reflectivity plot of $\text{Sm}_{1-x}\text{Y}_x\text{S}$ for $x = 0, 0.05, 0.17,$ and 0.33 . **b, c** Near-field imaging of a grating pattern on the surface of a $\text{Sm}_{0.83}\text{Y}_{0.17}\text{S}$ sample collected at 113 meV and 1.68 eV, respectively. The scale bars in both images are 1 μm . **d** Near-field imaging at 117 meV of micro-letters “SB” (Stony Brook) patterned on the surface of undoped SmS at room temperature subsequent to heat treatment at 333, 493, and 573 K. The solid white lines in the 493 K image indicate the number of lithographic lines required to produce the pattern in given areas. The scale bar is 1 μm . **e** A direct comparison of the near-field amplitude line profiles indicated by dashed white lines in **d**, is shown, highlighting the ability to tune the strength of the local IR reflectivity with temperature. **f** Height profile (blue line) and normalized near-field amplitude (gold line) of a lithographically patterned line (indicated by white arrows) at the center of the lithographic “S” in **d**. The FWHM is ~ 50 nm

a 20×20 lithographic grid with line spacing of 1 μm and a total area of $\sim 40 \times 40 \mu\text{m}$, while the grating MM is 10 parallel lines spaced 1 μm apart with a total area of $\sim 12 \times 12 \mu\text{m}$. Area-averaged far-field reflectance spectroscopy over a broad spectral range is performed using a gold film as a reference. The unpatterned semiconducting and metallic responses are consistent with previous reflectance measurements^{11,16}. In the semiconducting response, the reflectivity minimum at the low-energy side is the result of a plasma resonance coupled to an LO phonon mode¹¹. The presence of the tip-engineered MM dramatically increases the IR reflectance; further, a broad resonance appears centered near 0.21 eV (1700 cm^{-1}) in both MM while an additional resonance is evident at 0.5 eV (4000 cm^{-1}) for the fishnet only. The reflectance response of the four regions is simulated using Lichtenecker’s mixing rule based on the effective medium theory (EMT) for surface inclusions (Fig. 3b: dashed lines, see Supplementary Note 8 for details on the simulation method and parameters) that takes into consideration the metallic fill fraction as well as the shape of the metallic inclusions. The EMT fit shows good agreement with all of the far-field reflectance spectra, verifying that the broadband reflectivity increase is the result of the increased metallic volume fraction within the measurement area.

The IR resonance peaks, attributed to plasmonic shape effects, are characterized by simulating the reflectance in CST Microwave Studio as discussed in Supplementary Note 9. For the grating MM, the metallic area is an accurate representation of the experimental parameters. The simulated metallic area of the fishnet is smaller than the experimental conditions in order to save computational time, and the baseline reflectivity offset of the simulated fishnet response has been shifted up to account for the decrease in total metallic surface area compared to the actual MM pattern. The models reproduce these plasmonic resonances quite well, illustrating the two absorption features arise from the geometry of the MM.

Dopant and temperature tuning of the heavy fermion band.

Finally, in Fig. 4, we demonstrate the ability to tune the strain-engineered plasmonic responses with doping and temperature. Substitutional yttrium (Y) alters the optical properties of SmS, as can be seen in the far-field FTIR reflectivity spectra of Fig. 4a for $\text{Sm}_{1-x}\text{Y}_x\text{S}$ for $x = 0$ –33%. In undoped SmS, the 4f electron band is noticeable as a sharp resonance in the far IR. With increasing yttrium doping, this resonance essentially disappears as the 4f

band merges with the 5d conduction band, consistent with previous reports^{11,25}. Figure 4b and c show near-field images collected on a patterned yttrium-doped sample $\text{Sm}_{0.83}\text{Y}_{0.17}\text{S}$ in the IR and visible frequency ranges, respectively. In the IR image, collected at 113 meV, there is essentially no conductivity change between the patterned and unpatterned regions, in marked contrast to what was observed in the undoped SmS in Fig. 2d. On the other hand, the visible conductivity change between the patterned regions measured at 1.68 eV is as strong or stronger than what was observed in the undoped SmS sample in Fig. 2c. This ability to turn off the susceptibility of the IR resonance to pressure while maintaining or strengthening the visible is a direct result of the multi-band nature of heavy fermion compounds: the yttrium substitution alters the 4f electron levels, causing them to merge with the 5d conduction band^{26,27}.

The IR near-field images of the pre-patterned letters SB (initials of Stony Brook) are taken at 295 K after heat treatment at temperatures ranging from 295 to 573 K as shown in Fig. 4d. With increasing heat treatment temperature, it is clear that the IR contrast of the “SB” pattern at 117 meV is gradually disappearing. Figure 4e compares the near-field amplitude at the same location (indicated by dashed white lines) for four heat treatment temperatures, confirming the decrease in optical reflectivity. We attribute this thermal tunability to the reduced 4f–5d orbital overlap resulting from lattice expansion, which causes the system to return to the semiconducting phase¹⁴. Figure 4f compares the topography and near-field amplitude across the same lithographically fabricated line at room temperature (295 K), indicating the average FWHM of a typical patterned line before heat treatment. This ability to systematically reduce the reflectivity with thermal treatment opens the possibility of controlling the MM performance after the fabrication process is complete.

Discussion

In summary, our work demonstrates that the combination of ultra-broadband near-field and far-field characterization is appealing for studying correlated nanophotonics. The fine spatial resolution provided by s-SNOM enables the measurement of excitons at room temperature in the intermediate valence golden phase as well as incremental increases in the absorption edge across the black to golden transition, indicative of strongly localized 4f electrons moving into the 5d t_{2g} band. Access to the near- and far-field responses enables the ability to separately identify and tune the f and d electron contributions to the MM response. Further, substitutional doping of yttrium in place of the samarium ions makes it possible to effectively turn off the 4f plasmon resonance, leaving only the 5d electron resonance. Therefore, by strategically utilizing phase diagrams, highly tunable photonic devices can be created in correlated poor metals with extreme flexibility over a broad spectral range. This methodology can be generally applied to other pressure sensitive SCES such as Mott insulators (V_2O_3 ²⁸, Ca_2RuO_4 ²⁹), and high- T_c superconductors³⁰, where noble-metal structures can be incorporated into future designs to compensate for the losses induced by the heavy electrons.

Methods

Sample growth, patterning, and strain. The single-crystal materials were grown by the vertical Bridgman method in a high-frequency induction furnace. Further details on the growth and materials characterization can be found in Supplementary Note 1. The AFM lithography is discussed in Supplementary Note 2. For information on the applied force during AFM patterning and residual strain estimates, please see Supplementary Note 3.

Near-field characterization. To collect the near-field images and spectra, the following systems were used: NeaSpec NeaSNOM, NT-MDT NTEGRA-IR, and the Synchrotron Infrared Nano-Spectroscopy (SINS) beamline 5.4 at the Advanced

Light Source, Lawrence Berkeley National Laboratory. For the images, the metallic (patterned) signal was referenced to the semiconducting (unpatterned) response. The broadband spectra collected at ALS were normalized to a gold thin film. Details on the specific experimental near-field systems, along with information on the tuning of near-field properties with doping and temperature can be found in Supplementary Note 4.

Far-field characterization. Far-field microscopy at visible frequencies was performed with an optical microscope coupled to a fiber spectrometer. An FTIR at beamline 5.4 of the Advanced Light Source, Lawrence Berkeley National Laboratory, was used to determine the broadband IR response. Details on both can be found in Supplementary Notes 5 and 6.

Simulations. Supplementary Notes 7–9 contain details on the Drude and effective medium theory models, the fitting procedures used, as well as the IR reflectance simulations using the time-domain solver of Computer Simulation Technology (CST) microwave studio.

Data availability. The data that support the findings of this study are available from the corresponding authors (stephanie.gilbertcorder@stonybrook.edu and mengkun.liu@stonybrook.edu) upon request.

Received: 20 September 2017 Accepted: 22 November 2017

Published online: 22 December 2017

References

- Yu, N. & Capasso, F. Flat optics with designer metasurfaces. *Nat. Mater.* **13**, 139–150 (2014).
- Smith, D. R., Pendry, J. B. & Wiltshire, M. C. K. Metamaterials and negative refractive index. *Science* **305**, 788–792 (2004).
- Padilla, W. J., Basov, D. N. & Smith, D. R. Negative refractive index metamaterials. *Mater. Today* **9**, 28–35 (2006).
- Zheludev, N. I. A roadmap for metamaterials. *Opt. Photonics News* **22**, 30–35 (2011).
- Driscoll, T. et al. Memory metamaterials. *Science* **325**, 1518–1521 (2009).
- Rensberg, J. et al. Active optical metasurfaces based on defect-engineered phase-transition materials. *Nano Lett.* **16**, 1050–1055 (2016).
- Ishikawa, A. & Tanaka, T. Plasmon hybridization in graphene metamaterials. *Appl. Phys. Lett.* **102**, 253110 (2013).
- Sámson, Z. L. et al. Metamaterial electro-optic switch of nanoscale thickness. *Appl. Phys. Lett.* **96**, 3 (2010).
- Ricci, M., Orloff, N. & Anlage, S. M. Superconducting metamaterials. *Appl. Phys. Lett.* **87**, 3 (2005).
- Chen, H. T. et al. Tuning the resonance in high-temperature superconducting terahertz metamaterials. *Phys. Rev. Lett.* **105**, 4 (2010).
- Batlogg, B., Kaldis, E., Schlegel, A. & Wachter, P. Electronic structure of Sm monochalcogenides. *Phys. Rev. B* **14**, 5503–5514 (1976).
- Deen, P. P. et al. Structural and electronic transitions in the low-temperature, high-pressure phase of SmS. *Phys. Rev. B* **71**, 5 (2005).
- Mizuno, T. et al. Excitonic instability in the transition from the black phase to the golden phase of SmS under pressure investigated by infrared spectroscopy. *J. Phys. Soc. Jpn.* **77**, 4 (2008).
- Rogers, E. et al. The thermally induced metal-semiconducting phase transition of samarium monosulfide (SmS) thin films. *J. Phys. Condens. Matter* **22**, 7 (2010).
- Matsubayashi, K. et al. Effect of nominal composition on transport, optical, magnetic, and thermodynamic properties of SmS single crystals. *J. Phys. Soc. Jpn.* **76**, 6 (2007).
- Travaglini, G. & Wachter, P. Low-energy electronic structure of intermediate-valence ‘golden’ SmS. *Phys. Rev. B* **30**, 5877–5883 (1984).
- Jarrige, I. et al. Unified understanding of the valence transition in the rare-earth monochalcogenides under pressure. *Phys. Rev. B* **87**, 115107 (2015).
- Khomskii, D. Basic aspects of the quantum theory of solids (Cambridge University Press, New York, 2010).
- Cheng, G. et al. Sketched oxide single-electron transistor. *Nat. Nanotechnol.* **6**, 343–347 (2011).
- Huber, A. J., Ziegler, A., Köck, T. & Hillenbrand, R. Infrared nanoscopy of strained semiconductors. *Nat. Nanotechnol.* **4**, 153–157 (2009).
- Bechtel, H. A., Muller, E. A., Olmon, R. L., Martin, M. C. & Raschke, M. B. Ultrabroadband infrared nanospectroscopic imaging. *Proc. Natl Acad. Sci. USA* **111**, 7191–7196 (2014).
- Huth, F. et al. Nano-FTIR absorption spectroscopy of molecular fingerprints at 20 nm spatial resolution. *Nano Lett.* **12**, 3973–3978 (2012).

23. Govyadinov, A. A. et al. Quantitative measurement of local infrared absorption and dielectric function with tip-enhanced near-field microscopy. *J. Phys. Chem. Lett.* **4**, 1526–1531 (2013).
24. Kang, C.-J., Choi, H. C., Kim, K. & Min, B. I. Topological properties and the dynamical crossover from mixed-valence to kondo-lattice behavior in the golden phase of SmS. *Phys. Rev. Lett.* **114**, 166404 (2015).
25. Güntherodt, G. & Holtzberg, F. Optical studies of semiconductor to metal transition in Sm_{1-x}Y_xS. *AIP Conf. Proc.* **24**, 36–37 (1975).
26. Güntherodt, G., Jayaraman, A., Anastassakis, E., Bucher, E. & Bach, H. Effect of configuration crossover on the electronic Raman scattering by 4f multiplets. *Phys. Rev. Lett.* **46**, 855–858 (1981).
27. Freeouf, J. L., Eastman, D. E., Grobman, W. D., Holtzberg, F. & Torrance, J. B. Spectroscopically observed valence mixing in SmS and related compounds. *Phys. Rev. Lett.* **33**, 161–164 (1974).
28. Limelette, P. et al. Universality and critical behavior at the mott transition. *Science* **302**, 89 (2003).
29. Nakamura, F. et al. From mott insulator to ferromagnetic metal: a pressure study of Ca₂RuO₄. *Phys. Rev. B* **65**, 4 (2002).
30. Tosatti, E. Superconductivity: squash and sandwiches. *Nat. Mater.* **7**, 929–930 (2008).

Acknowledgements

We gratefully acknowledge the efforts of M. Raschke and his group in developing the SINS instrument at the Advanced Light Source and also G.L. Carr (Brookhaven National Lab) for the custom Cu:Ge detector provided as part of the NSLS-II remote IR program at ALS under the US Department of Energy Contract No. DE-SC0012704. The Advanced Light Source is supported by the Director, Office of Science, Office of Basic Energy Sciences, of the US Department of Energy under Contract No. DE-AC02-05CH11231. K. I. and N.K.S. acknowledge the Program for Leading Graduate Schools Integrative Graduate Education and Research Program in Green Natural Sciences, MEXT, Japan and the Grant-in-Aid for Scientific Research from JSPS, KAKENHI (nos 26870265 and 15H02111). T.H.T. and M.K.L. acknowledge support from the NSF-CMMI under grant nos. 1563422 and 1562915. Work at Texas A&M University is supported by the Army Research Office grant 68170-PH.

Author contributions

S.N.G.C., X.C., S.Z., F.H., J.Z., Y.L., and M.K.L. contributed to near-field data collection. S.N.G.C., T.C., S.K., T.I., and K.I. performed far-field data collection. S.N.G.C., S.Z., J.Z., J.A.L., and M.K.L. fabricated the MM patterns. X.C. performed the CST simulations. M. A., H.S.S., K.I., and N.K.S. supplied the sample materials. Z.F., H.A.B., M.C.M., T.H.T., and M.K.L. provided access to the equipments used in this work. S.N.G.C. and M.K.L. wrote the manuscript. All authors contributed to the editing of the manuscript.

Additional information

Supplementary Information accompanies this paper at <https://doi.org/10.1038/s41467-017-02378-3>.

Competing interests: The authors declare no competing financial interests.

Reprints and permission information is available online at <http://npg.nature.com/reprintsandpermissions/>

Publisher's note: Springer Nature remains neutral with regard to jurisdictional claims in published maps and institutional affiliations.



Open Access This article is licensed under a Creative Commons Attribution 4.0 International License, which permits use, sharing, adaptation, distribution and reproduction in any medium or format, as long as you give appropriate credit to the original author(s) and the source, provide a link to the Creative Commons license, and indicate if changes were made. The images or other third party material in this article are included in the article's Creative Commons license, unless indicated otherwise in a credit line to the material. If material is not included in the article's Creative Commons license and your intended use is not permitted by statutory regulation or exceeds the permitted use, you will need to obtain permission directly from the copyright holder. To view a copy of this license, visit <http://creativecommons.org/licenses/by/4.0/>.

© The Author(s) 2017